Iraqi Journal of Physics, 2024 *Vol. 22, No. 2, PP. 69-80*
https://doi.org/10.30723/ijp.v22i2.1169 *P-ISSN: 2070-4003*
E-ISSN: 2664-5548

Influence of Laser Energy on the Structural and Optical Properties of Sn Nanoparticles produced with Laser-Induced Plasma

Raghad T. Ahmed[1a*] and Ala F. Ahmed[2b]
[1]*Department of Physics, College of Science, University of Baghdad, Baghdad, Iraq*
[2]*Department of Astronomy & Space, College of Science, University of Baghdad, Baghdad, Iraq*
[b]E-mail: ala.ahmed@sc.uobaghdad.edu.iq
[a*]Corresponding author: raghda@bauc14.edu.iq

Abstract

This study aimed to investigate the structure and optical properties of Sn nanostructures. Thin tin (Sn) films were deposited on glass substrates using the pulsed laser deposition method. Nd:YAG laser with fundamental wavelengths of 532 nm and 1064 nm was used to create Sn nanostructures with varying energies of 400 mJ to 700 mJ and the same frequency of 6 Hz. The tin powder was compressed into a disc with a one-centimetre diameter to serve as a sample. The X-ray diffraction (XRD) pattern showed a crystalline structure with several Sn nanostructures peaks at various energies (400–700 mJ). The results revealed a crystalline size of 65.90 nm and 86.55 nm at 700 mJ, while the size was 40.19 nm and 17.19 at 400 mJ for the given wavelengths (532nm and 1064 nm), respectively. The appearance of Sn nanostructures and the aggregation of, particularly in the form of cauliflower, were revealed in Field emission scanning electron microscopy (FE-SEM) images. The results of the dispersive energy X-ray spectroscopy (EDS) analysis showed that various amounts of tin, carbon, and oxygen were present. Additionally, the optical characteristics were investigated of each film using absorbance spectra, which covered a range of wavelengths from 190 to 1100 nm. As the laser power increased, the band gap energy values in the optical properties decreased, falling into the ranges of 3.06 to 1.65 eV and 3.22 to 1.82 eV at 1064nm and 532nm, respectively.

Article Info.

Keywords:
Laser-Induced Plasma, Sn, XRD, AFM, Energy Gap.

Article history:
Received: Jul. 08, 2023
Revised: Dec. 18, 2024
Accepted: Feb. 19, 2024
Published: Jun. 01, 2024

1. Introduction

High-power lasers find applications in various fields, such as the pulsed laser deposition (PLD) of thin films, laser-assisted machining, laser diagnostics, and elemental trace analysis [1]. In these processes, the laser beam interacts with the target material, causing dissipations and ionizations, thereby creating a plasma plume above the target's surface [2]. It is essential to comprehend the transport mechanism of the laser beam within the laser-induced plasma plume. This understanding is crucial for effectively controlling the interaction between the laser and the materials being used, as well as for optimizing high-power laser processes [3, 4]. The formation of laser-induced plasma involves five distinct processes: excitation, ionization, dispersion, dissolving, and heating. Initially, high-energy laser pulses emitted from a Q-switched laser source are directed onto a solid or liquid surface [5] or a small volume of a gas sample using an appropriate lens [6, 7]. This focused laser beam induces excitation and ionization of the target material, leading to the formation of a plasma plume [8]. This plume consists of a mixture of electrons, neutral atoms, and ions, which are rich in energy [9]. Subsequently, the temperature of the region involved in the process experiences rapid and significant elevation, reaching the threshold required for vaporization [10]. Applications of laser-induced plasma have currently spread to numerous fields for elemental composition determination of products [11], biomedical applications [12], geological studies [13], mineral mining process control [14], etc.

Tin (Se) is a unique semiconductor material of tetragonal structure with an energy gap of about 3.6 eV [15, 16].

The aims of this project are to produce tin nanostructures and investigate the influnce of laser energy on structural and optical characteristics of these nanostructures.

2. Experimental Work

PLD method is typically conducted in a pressure vacuum chamber with a pressure of 2.5×10^{-2} mbar. A solid tin disc measuring 1 cm in diameter and 0.2 cm in thickness was prepared by compressing 2 g of Sn nanostructures powder using a Specac hydraulic press under a pressure of 6 tons for 10 min. To deposit tin nanostructures, Nd:YAG laser with a repetition rate of 6 Hz and different laser energies of 400, 500, 600, and 700mJ was employed. The laser emitted 200 pulses and operated at wavelengths of 532 nm and 1064 nm. The incident Nd:YAG Q-switching laser beam was directed to the target surface at an angle of approximately 45^{o}. The experimental setup consisted of vacuum systems, as shown in Fig.1. The synthesized Sn structures were characterized at the University of Kashan, Iran employing X-ray diffraction (XRD) (using PANalytical XPert diffractometer, Phillippines), field emission scanning electron microscopy (FE-SEM), dispersive energy X-ray spectroscopy (EDS) (Tescan MIRA3, France), and Transmission electron microscopy (TEM) techniques.

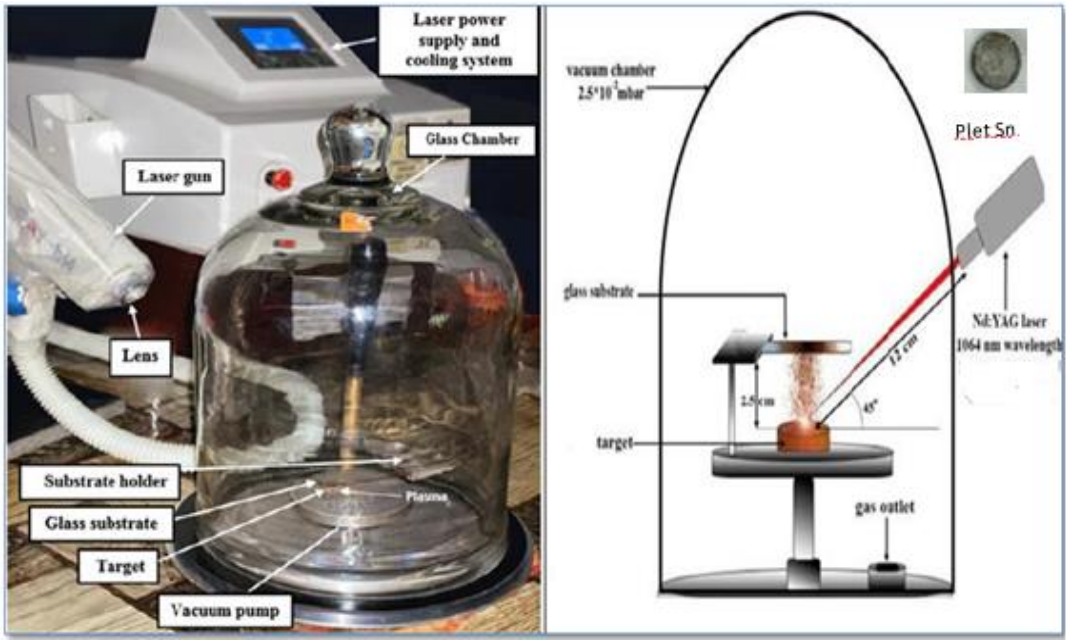

Figure 1: PLD system using Nd:YAG with wavelength 1064nm and 532nm [17].

2. Results and Discussion

3.1 X-ray Diffraction Analysis (XRD)

Figs. 2 and 3 depict the XRD patterns of Sn nanostructure prepared with various laser energies. All samples showed polycrystalline tetragonal structures that matched the standard card (No. 00-004-0673). The XRD of Sn nanostructure prepared using 332nm laser of 400 and 700 mJ energies, shown in Fig. 2, showed many peaks at diffraction angles (2θ) of 30.64°, 32.01°, 44.7°, 44.95°, 56.47°, and 63.55° indicating the lattice planes (200), (101), (220), (211), (301), and (112), respectively. Using the 1064nm laser of 400 and 700 mJ energies, the XRD pattern showed peaks at diffraction angles (2θ) 30.64°, 32.01°, 44.7°, and 44.95° corresponding to (200), (101), (220), and (211) lattice planes, respectively. Changes in the positions of the peaks with increasing

laser energy were noted due to the difference in the lattice uniform strain with variation in crystalline size [18]. It is also evident that the peaks intensity increased while the width of the peaks decreased with increasing the laser energy, indicating increased crystallinity and growing crystalline size. When the laser power increases, the size of the crystals increases, which leads to the removal of larger masses of the target material. Also, high laser power leads to the merging of small particles with each other [3, 17]. The XRD peak intensity using the 1064 nm laser was higher than that of the 532 nm laser at the same laser energy. The interaction between the 532 nm wavelength laser and the target is less due to less surface absorption. This means that the target absorbs more energy from the 532 nm laser, resulting in less energy available for scattering and generating X-ray diffraction signals. In contrast, the 1064 nm laser is absorbed less, allowing more energy to contribute to the diffraction signal and leading to higher peak intensity.

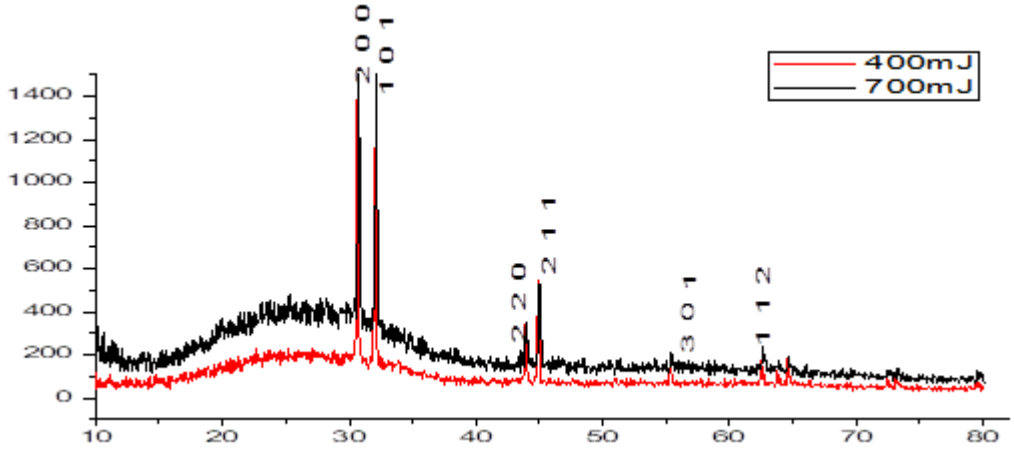

Figure 2: XRD pattern of Sn nanostructure at λ=532 nm.

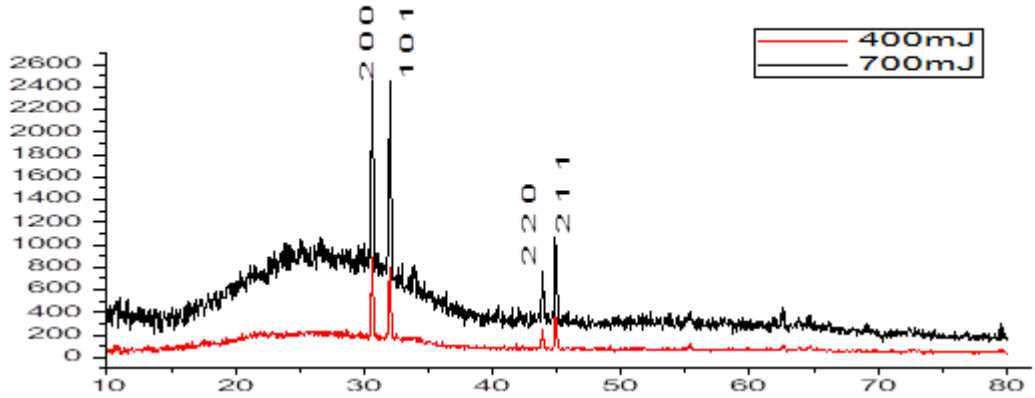

Figure 3: XRD pattern of Sn nanostructure at λ=1064 nm.

The crystal structure, orientation, and grain size of a material may be identified by the use of XRD [19], which is a potent, non-destructive approach to material characterization. Scherer's formula was used to determine how large the individual crystals are (D) in a polycrystalline film [9, 20]:

$$D = \frac{K\lambda}{\beta COS(\theta)} \qquad (1)$$

The full width at half maximum (β) is a measure of the angular width of the peak in a diffraction pattern, expressed in radians [21, 22], and the Bragg angle (θ) is the angle at

which constructive interference occurs in a crystal lattice related to the diffraction of X-ray or other radiation. Cu (ka) radiation was employed as the radiation source, with a wavelength of 1.5406 Å. Table 1 provides the diffraction parameters for Sn thin films that were prepared using different laser energies and their corresponding intensities.

Table 1: The variation of XRD parameters for Sn nanostructure at different laser energies.

E (mJ)	2θ (Deg.)	FWHM(nm)	C.S (nm)	Av. C.S(nm)	hkl
			λ=532nm		
400mJ	30.64616	0.19251	44.76	21.82	(200)
	32.01819	0.1649	52.37		(101)
	43.76879	0.473	18.86		(220)
	44.95589	0.715	12.52		(211)
	56.47776	8.33885	1.14		(301)
	63.55797	7.639318	1.28		(112)
700mJ	30.64616	0.1476	58.46	36.22	(200)
	32.01819	0.235	36.75		(101)
	43.76879	0.1968	45.52		(220)
	44.95589	0.3678	24.87		(211)
	56.47776	0.278	33.82		(301)
	63.55797	0.543	17.93		(211)
			λ=1064nmm		
400mJ	30.05307	0.96757	8.95	18.17	(200)
	32.01944	0.16199	53.987		(101)
	43.6325	1.79707	5.05		(220)
	44.38416	1.9	4.72		(211)
700mJ	30.36936	6.32485	1.36	27.91	(200)
	32.09302	0.658	13.20		(101)
	43.76881	0.221	27.71		(220)
	44.81532	0.129	69.40		(211)

3.2. Atomic Force Microscope Analysis (AFM)

Atomic Force Microscope Analysis (AFM) is an essential instrument for the characterization of nanoparticles. AFM can achieve spatial resolutions of less than one nanometer because it images samples using electrons rather than photons [23]. Figs. 4 and 5 illustrate AFM images obtained with pulse laser energies of 400 mJ and 700 mJ, respectively. In both cases, the AFM images reveal a uniform surface with strong adhesion to the glass substrate.

It should be noted that the nanostructure surface exhibits variations as a consequence of different laser energy levels, as demonstrated in Table 2. Specifically, as the laser energy increased from 400 mJ and 700 mJ the granular size of the nanostructure increased. This indicates that higher laser energies result in a higher proportion of scouring, contributing to larger granules on the surface. During the deposition process, the migration of nanostructure layers towards the surface occurs through interactions with the ablation products present in the plasma. These ablation products comprise both ions and uncharged ablation fractions, each with distinct diffusion rates. Ions, characterized by their high energies or speeds, exhibit rapid movement. On the other hand, the velocity of uncharged fragments depends on their frequency of collisions with charged particles. Consequently, when the laser intensity is increased, leading to more pronounced excision or removal, there is an elevated likelihood of larger granules appearing on the surface due to multiple impacts. This, in turn, leads to an increase in surface roughness of the nanostructure. The observations

made through atomic force microscopy are in agreement with the findings reported by de Haan et al. [23] and Hasaneen et al. [24].

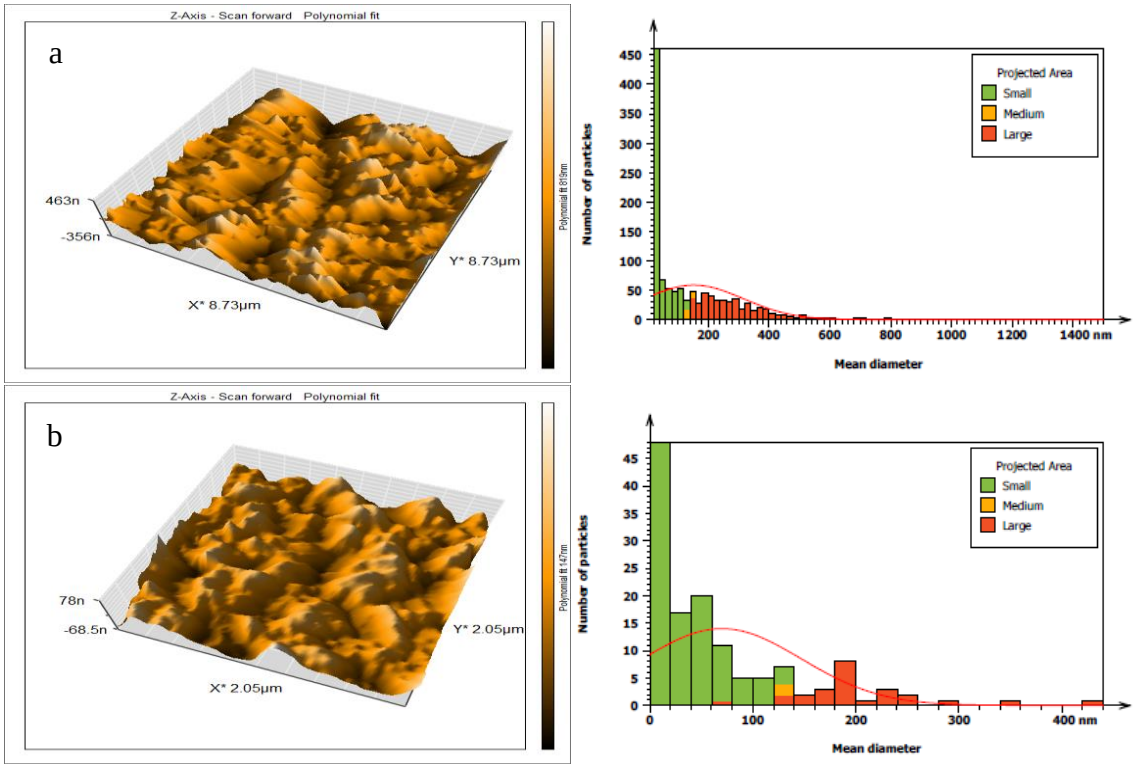

Figure 4: 3D AFM for Sn nanostructure prepared by PLA with(a) 400 mJ laser energy (b)700mJ and granularity accumulation distribution at λ=532nm.

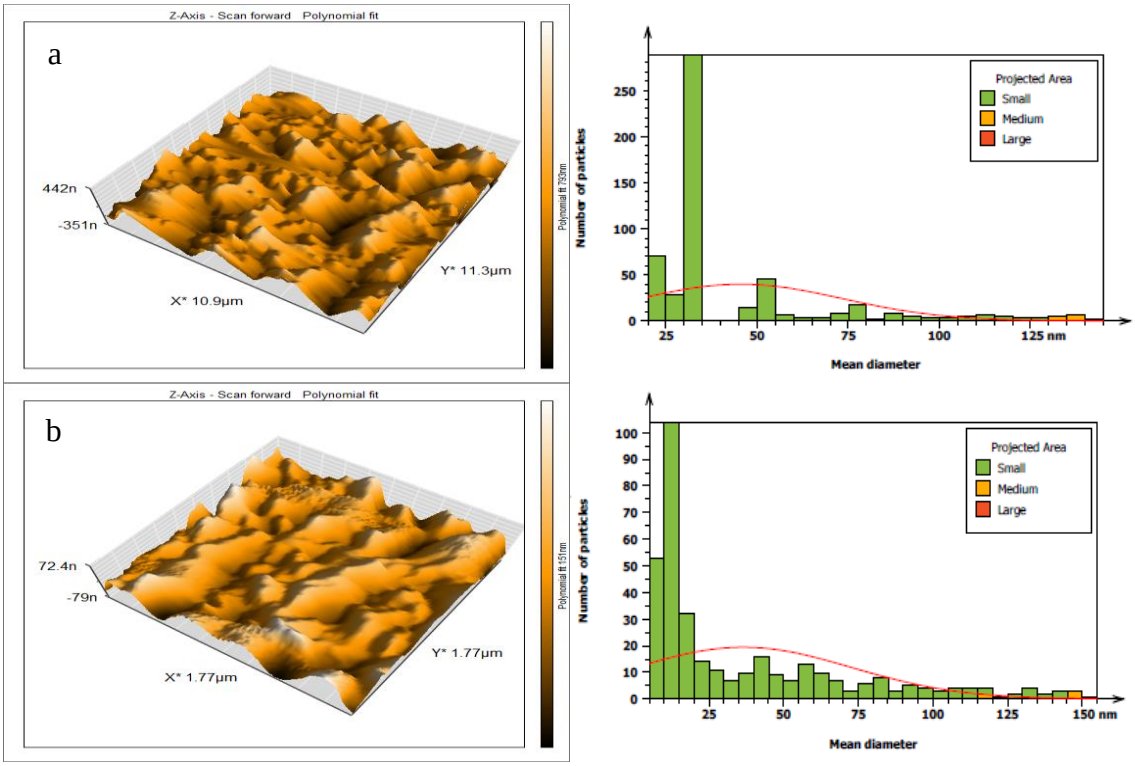

Figure 5: 3D AFM for Sn nanostructure prepared by PLA with(a) 400 mJ laser energy (b)700mJ and granularity accumulation distribution at λ=1064nm.

Table 2: AFM parameters for Sn films with different laser energies.

E(mJ)	Ave. Roughness (nm)	Root Mean Sq. (nm)	Ave. diameter (nm)
Sn-λ=532nm			
400mJ	38.32	33.37	153.1
700mJ	27.45	46.22	70.02
Sn-λ=1064nm			
400mJ	39.02	49.69	87.56
700mJ	109.2	134.9	79.92

3.3. Field Emission Scanning Electron Microscopy (FE-SEM)

Figs. 6 and 7 show the surface morphology of SnNPs. The FESEM images revealed the agglomeration of NPs due to their attractive forces. The FESEM images depict Sn thin coatings on glass substrates prepared using different laser energies, indicating uniform deposition, covering the entire substrate in a cauliflower-shaped pattern. With increasing laser energy, the particle density increased due to the merging of adjacent particles, leading to a more solid appearance and reduced vacancies. It is important to note that the merging of adjacent particles and the resulting reduction in vacancies may affect the optical properties of the Sn films, as observed in the analysis of the band gap energy values. Overall, the FESEM images provide valuable information on the surface morphology and changes in density and particle size of the Sn films with varying laser energy [25].

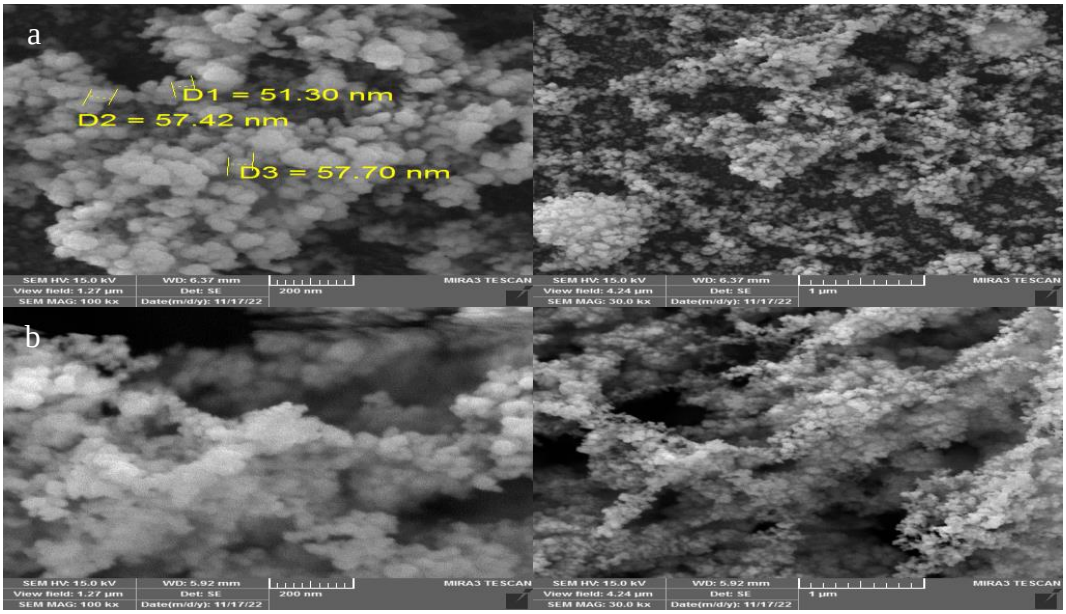

Figure 6: FE-SEM images of Sn NPs measurement at range (200nm and 1 μm) with laser energy (a) 400mJ and (b) 700mJ at λ=532nm.

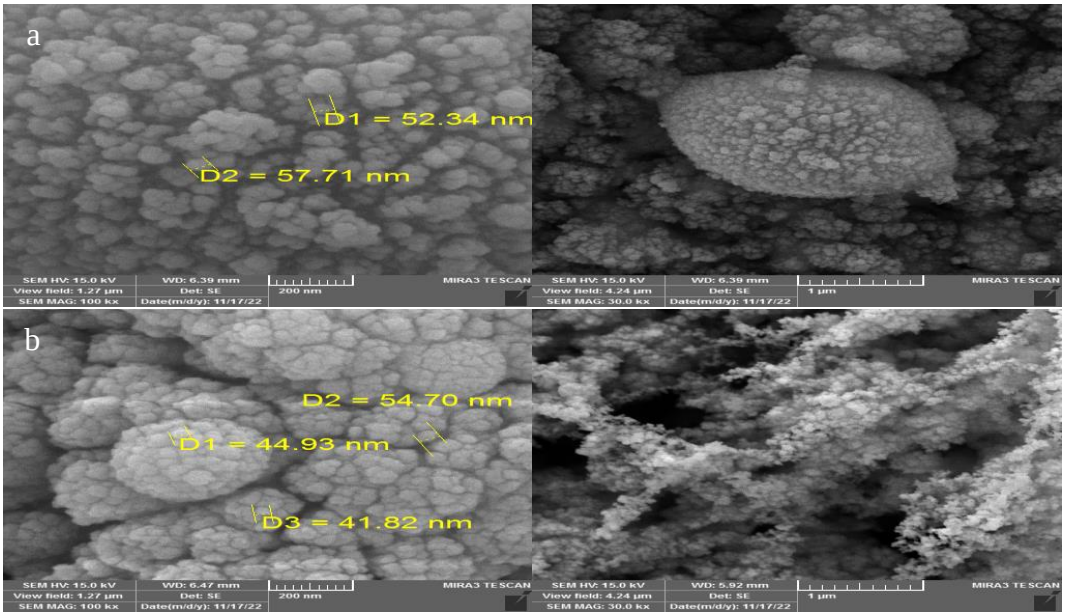

Figure 7: FE-SEM images of Sn NPs measurement at range (200nm and 1 μm) with laser energy (a) 400mJ and (b) 700mJ at λ=1064nm.

3.4. Energy Dispersive X-Ray Spectroscopy (EDS)

Dispersive Energy X-ray spectroscopy (EDS) is a commonly used technique to analyze and quantify the elemental composition of a small material sample. In EDS, an electron beam is directed at the surface of the sample, which results in the excitation of surface atoms. These excited atoms emit X-rays that are specific to the atomic structure of each element present in the sample. By measuring and analyzing these emitted X-rays, the elemental composition of the sample can be determined. Figs. 8 and 9 illustrate the presence of Sn atoms. In terms of weight % and atomic %, the compositional percentages of Sn, C (carbon), and O (oxygen) are depicted.

The vertical axis of the figures represents the quantity of X-ray counts, while the horizontal axis represents the energy of the X-rays in keV. The figures provide insights into the relative amounts of Sn, C, and O elements in the sample, as determined by EDS analysis.

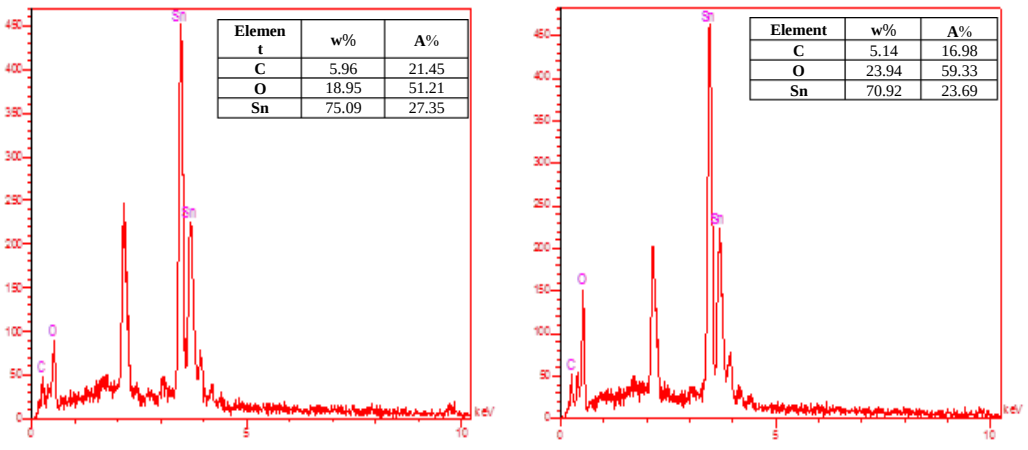

Figure 8: EDS spectra of Sn nanoparticles prepared at laser energies of 400 and 700 mJ at λ=532nnm.

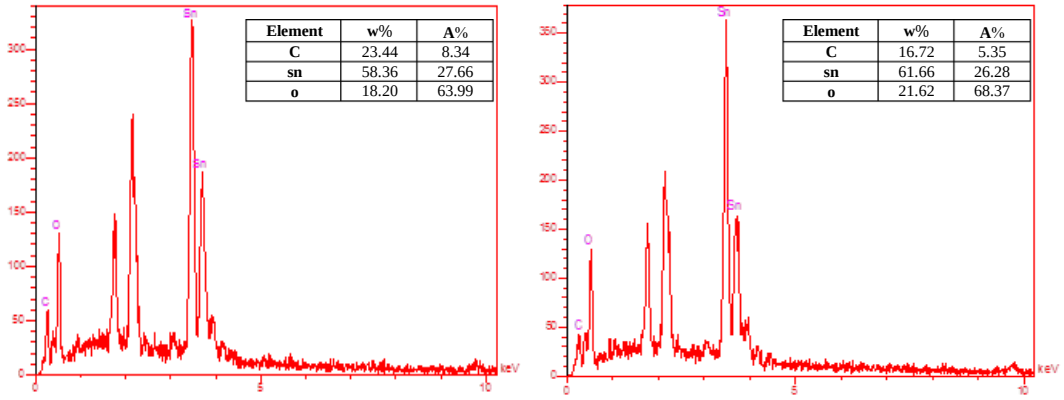

Figure 9: EDS spectra of sn nanoparticles prepared at laser energies of 400 and 700 mJ at λ=1064nm.

3.5. Optical Properties

The optical properties of Sn nanostructures on glass substrates at room temperature were studied at different laser energies. The optical characteristics of the nanostructures were then analyzed using UV-Vis spectroscopy.

3.5.1. The Absorbance Spectrum (A)

Fig. 10 presents the optical absorption spectra of Sn nanostructures at various laser energies ranging from 400 mJ to 700 mJ. The absorption peaks were observed within specific wavelength ranges, namely 280 nm to 888 nm for 532 nm laser and 1064 nm laser. Analyzing the absorption spectrum depicted in Fig. 10, it is evident that the absorbance increases with the increase of the energy of the laser pulse. This can be attributed to a higher proportion of scraping, leading to an increased grain size rate. Consequently, the surface roughness increases, resulting in greater absorption of photons. As the wavelength increases, photons lose energy and become less capable of interacting with matter's atoms. Consequently, photons undergo scattering processes. The relationship between surface roughness and absorption is in accordance with the findings of Frit et al. [26].

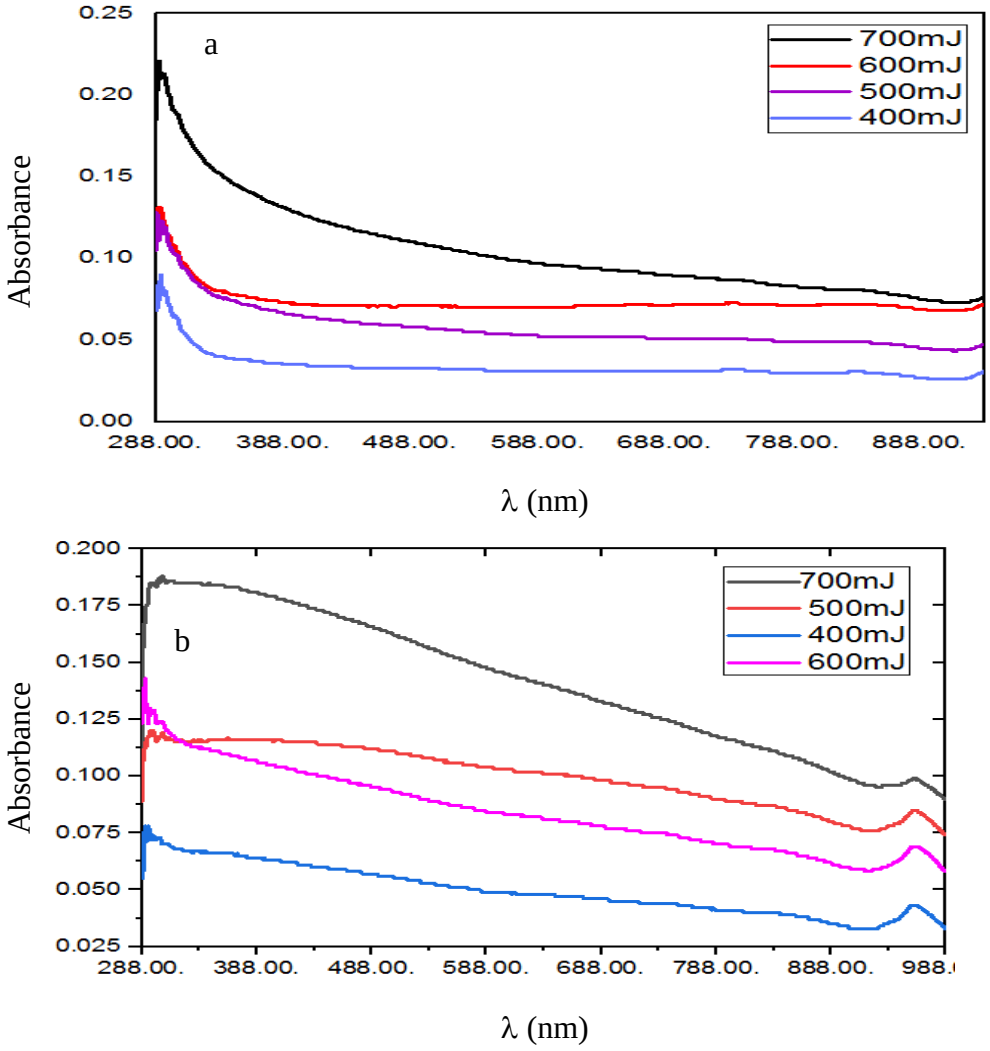

Figure 10: Absorbance spectra of Sn nanostructures as a function of wavelength at different laser energies using (a) 532nm and (b) 1064nm.

3.5.2. Optical Energy Band Gap (E_g)

The optical band gap energy, represented by the symbol E_g, is a highly significant optical constant in semiconductor physics. This parameter is essential in determining the applicability of semiconductors in a wide range of optical and electrical applications [27]. The value of E_g is influenced by the crystal structure of the material, which implies that it is sensitive to the particular arrangement of atoms within the semiconductor [28]. Knowledge of the absorption coefficient (A) and the incident photon's energy (hυ) is necessary to determine the value of E_g. When converting (αhν) 2×10^{11} $(eV \cdot cm^{-1})^2$ to energy units from wavelength units, the plotted value represents the amount of energy absorbed by the material per unit wavelength (cm^{-1}) as a function of the square of the absorption coefficient. Utilizing appropriate formulas, the value of the band gap energy can be calculated[29]:

$$(h\upsilon) = A\,(h\upsilon - E_g)^{r} \qquad (2)$$

According to the provided information, Figs. 11 and 12 were utilized to determine the band gap energy values for Sn films deposited on glass substrates. The laser pulse energy used for the deposition varied from 400 mJ to 700 mJ. The results in Table 3 indicate that the band gap energy values ranged from (3.06 to 1.65) eV and (3.22 to

1.82) eV at 1064nm and 532nm, respectively. The decrease in band gap energy values with increasing laser pulse energy suggests an increase in the particle size of the Sn films. This observation is attributed to the presence of secondary levels within the band gap, which results in the widening of the energy difference. Consequently, more granules or particles are observed on the surface of the glass slide. These findings are consistent with the results reported by Faiadh [30]. The laser energy that excites the Sn nanoparticles can affect their optical properties, including the band gap energy. Higher laser energies can induce changes in the electronic structure of the nanoparticles, such as excited state transitions or energy transfer processes, which can contribute to a decrease in the band gap energy values.

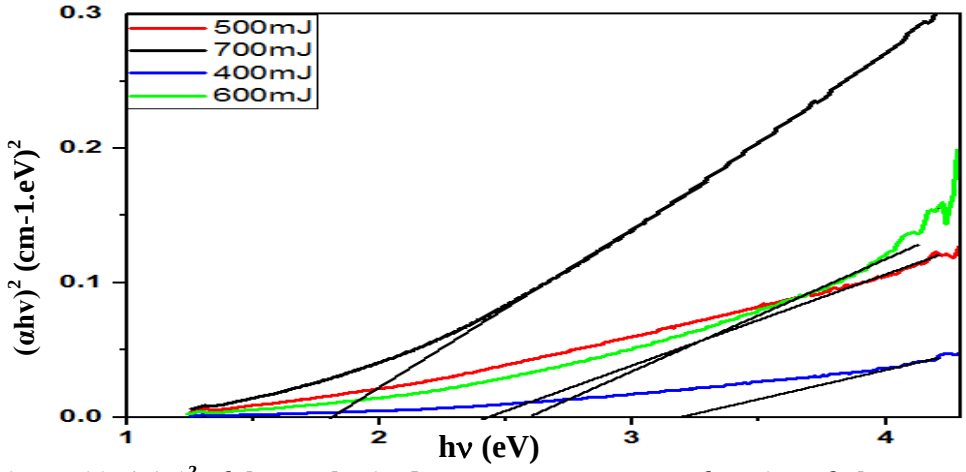

Figure 11: $(\alpha h\nu)^2$ of the synthesized Sn nanostructure as a function of photon energy at various laser energies with 532nm laser wavelength.

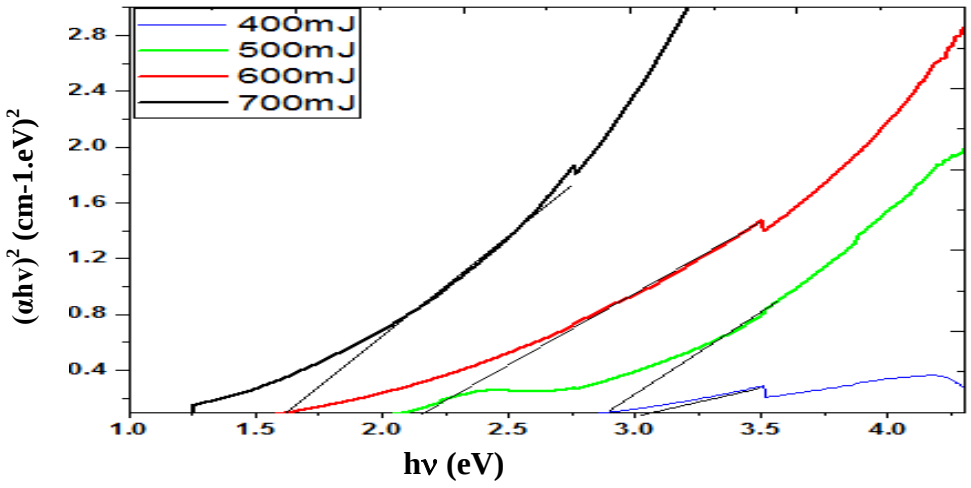

Figure 12: $(\alpha h\nu)^2$ of the synthesized Sn nanostructures as a function of photon energy at various laser energies with 1064nm laser wavelength.

Table 3: Effect of laser energy on the optical band gap energy of the Sn nanostructure.

Laser energy (mJ)	Band gap energy	
	λ=532nm	λ=1064nm
400	3.22	3.06
500	2.62	2.91
600	2.43	2.19
700	1.82	1.65

4. Conclusions

Se nanostructures were synthesized using laser-induced plasma employing two laser wavelengths of 532nm and 1064 nm with varying laser energies ranging from 400 to 700 mJ and 200 pulses. XRD analysis confirmed that the resulting polycrystalline films exhibited a tetragonal structure. Furthermore, the experimental data indicated that the grain size increased with the laser energy, increasing average roughness. The FE-SEM images provided visual evidence of the nanoparticle morphology and the agglomeration of Sn nanostructures, which appeared in a cauliflower-like formation. Moreover, the investigation of the Sn nanostructure's optical properties revealed that an increased in laser energy decreased the band gap energy.

Acknowledgments

The authors would like to thank the University of Baghdad, College of Science, Department of Physics for their assistance in carrying out this work.

Conflict of interest

The authors declare that they have no conflict of interest.

References

1. T. Ma, Ph.D Thesis, The University of Hong Kong, 2004.
2. Y. Zhang, T. Zhang, and H. Li, Spectrochim. Acta Part B Atomic Spectro. **181**, 106218 (2021).
3. D. Zhang, Y. Chu, S. Ma, Z. Sheng, F. Chen, Z. Hu, S. Zhang, B. Wang, and L. Guo, Appl. Surf. Sci. **534**, 147601 (2020).
4. U. H. Tawfeeq, A. K. Abbas, and K. A. Aadim, Journal of Physics: Conference Series (Istanbul, Turkey IOP Publishing, 2021). p. 012049.
5. S. Das, R. Bhunia, S. Hussain, R. Bhar, B. Chakraborty, and A. Pal, Appl. Surf. Sci. **353**, 439 (2015).
6. M. S. Nek, Y. Tao, R. A. Burdt, S. Yuspeh, N. Amin, and M. S. Tillack, J. Phys. Conf. Ser. **244**, 042005 (2010).
7. A. Ahmed, M. Salman, M. Alwazzan, and A. Meri, J. Adv. Res. Dyn. Control Syst. **11**, 412 (2019).
8. A. M. A. Hussein, S. A. Abdullah, M. Rasheed, and R. S. Zamel, Iraqi J. Phys. **18**, 73 (2020).
9. I. K. Abbas and K. A. Aadim, Sci. Tech. Indonesia **7**, 427 (2022).
10. E. Asamoah and Y. Hongbing, Appl. Phys. B **123**, 1 (2017).
11. F. Ruan, T. Zhang, and H. Li, Appl. Spect. Rev. **54**, 573 (2019).
12. Z. L. Petrović, N. Puač, S. Lazović, D. Maletić, K. Spasić, and G. Malović, Journal of Physics: Conference Series (Sunny Beach, Bulgaria IOP Publishing, 2012). p. 012001.
13. A. K. Rao and D. R. Kumar, Mat. Today Proce. **27**, 1768 (2020).
14. A. K. Myakalwar, C. Sandoval, M. Velásquez, D. Sbarbaro, B. Sepúlveda, and J. Yáñez, Minerals **11**, 1073 (2021).
15. S. Tazikeh, A. Akbari, A. Talebi, and E. Talebi, Mat. Sci. Poland **32**, 98 (2014).
16. O. A. Thuhaib and H. Hashim, Al-Nahrain J. Sci. **24**, 26 (2021).
17. N. K. Abdalameer, Ph.D Thesis, University of Baghdad, 2021.
18. D. Bhattacharya, Pramana **55**, 823 (2000).
19. S. M. Jafari, *Characterization of nanoencapsulated food ingredients* (London, UK, Academic Press, 2020).
20. E. J. Mohammed, A. K. Abbas, and K. A. Aadim, Iraqi J. Phys. **18**, 21 (2020).

21. M. V. Allmen and A. Blatter, *Laser-Beam Interactions with Materials: Physical Principles and Applications* (New York, Springer Science & Business Media, 2013).
22. Y. Shadangi, V. Shivam, M. K. Singh, K. Chattopadhyay, J. Basu, and N. Mukhopadhyay, J. All. Comp. **797**, 1280 (2019).
23. K. De Haan, Z. S. Ballard, Y. Rivenson, Y. Wu, and A. Ozcan, Sci. Rep. **9**, 12050 (2019).
24. M. Hasaneen, M. Shalaby, N. Yousif, A. Diab, and E. El Agammy, Mat. Sci. Eng. B **280**, 115703 (2022).
25. R. Indirajith, M. Rajalakshmi, K. Ramamurthi, M. B. Ahamed, and R. Gopalakrishnan, Ferroelectrics **467**, 13 (2014).
26. A. P. Frit, K. Deepalakshmi, N. Prithivikumaran, and N. Jeyakumaran, J. Chem. Tech. Res. **6**, 5347 (2014).
27. B. Zheng, J. Lian, L. Zhao, and Q. Jiang, Vacuum **85**, 861 (2011).
28. T. S. Hussein and A. F. Ahmed, Journal of Physics: Conference Series (IOP Publishing, 2021). p. 012012.
29. T. S. Hussein, A. F. Ahmed, and K. A. Aadim, Iraqi J. Sci. **63**, 548 (2022).
30. A. F. Ahmed, F. a.-H. Mutlak, and Q. A. Abbas, Appl. Phys. A **128**, 147 (2022).

تأثير طاقة الليزر على الخصائص التركيبية والبصرية للقصدير المحضرة بالبلازما المحتثة بالليزر

رغدة طلال احمد[1] والاء فاضل احمد[2]
[1] قسم الفيزياء، كلية العلوم، جامعة بغداد، بغداد، العراق
[1] قسم الفلك والفضاء، كلية العلوم، جامعة بغداد، بغداد، العراق

الخلاصة

في هذا العمل تم دراسة الخصائص التركيبية والبصرية للبنية النانوية Sn. تم تحضير الأغشية الرقيقة المترسبة على ركائز زجاجية عن طريق الترسيب بالليزر النبضي Nd: YAG بطول موجي أساسي من 532-1064 نانومتر لصنع Sn مع طاقات مختلفة (400-700 مللي جول) وبنفس التردد (6 هرتز). تم ضغط مسحوق القصدير في قرص يبلغ قطره سنتيمترًا واحدًا. أظهر نمط حيود الأشعة السينية (XRD) بنية بلورية وقممًا متعددة تتوافق مع Sn بطاقة مختلفة (400-700 مللي جول). كشفت النتائج عن حجم بلوري 65.90 نانومتر و86.55 نانومتر عند 700 مللي جول بينما كان الحجم 40.19 نانومتر و17.19 نانومتر عند 400 مللي جول للأطوال الموجية المعطاة (532-1064 نانومتر) على التوالي. تم عرض ظهور الجسيمات النانوية وتجمع Sn، لا سيما في شكل القرنبيط، في الصور التي تم الحصول عليها باستخدام FE-SEM. أظهرت نتائج تحليل EDX وجود كميات مختلفة من القصدير والكربون والأكسجين. بالإضافة إلى ذلك، تم فحص الخصائص البصرية لكل فيلم باستخدام طيف امتصاص يغطي مدى أطوال موجية من 190 إلى 1100 نانومتر. مع زيادة قوة الليزر، ستصبح قيم فجوة الطاقة في الخواص البصرية أصغر، حيث تقع في نطاقات (2.1 إلى 3.2) فولت و (1.55 إلى 3.1) فولت عند 532 نانومتر و1064 نانومتر، على التوالي

الكلمات المفتاحية: بلازما المحتثة بالليزر، القصدير، حيود الاشعة السينية، مجهر القوة الذرية، فجوة الطاقة